

Teleporting two-qubit entanglement across 19 qubits on a superconducting quantum computer

Haiyue Kang,^{1,*} John F. Kam,^{2,†} Gary J. Mooney,^{1,‡} and Lloyd C. L. Hollenberg^{1,§}

¹*School of Physics, The University of Melbourne, Parkville, Victoria 3010, Australia*

²*School of Physics & Astronomy, Monash University, Clayton, Victoria 3800, Australia*

(Dated: July 4, 2024)

Quantum teleportation is not merely a fascinating corollary of quantum entanglement, it also finds utility in quantum processing and circuit compilation. In this paper, we measure and track the entanglement and fidelity of two-qubit states prepared on a 127-qubit IBM Quantum device, as one of the qubits is teleported across 19 qubits. We design, evaluate and compare two distinct approaches to teleportation: post-selected measurement categorisation and dynamic circuit corrections based on mid-circuit measurements, and compare with direct state transportation using SWAP gates. By optimally choosing the teleportation path which exhibits the highest total negativity entanglement measure across nearest-neighbour pairs, we show the entanglement of a two-qubit graph state is sustained after at least 19 hops in teleportation using the post-selection approach and 17 hops using the dynamic circuit approach. We observe a higher level of teleported entanglement in paths determined from two-qubit negativities compared to those obtained from gate errors, demonstrating an advantage in using the negativity map over the gate error map for compiling quantum circuits.

I. INTRODUCTION

To fully unleash the potential of quantum algorithms that cannot be time-efficiently executed classically and have applications in many fields [1–9], the generation of large-scale entanglement on real quantum devices is an essential prerequisite. Hence, to demonstrate the utility of quantum computers, the generation and verification of large-scale quantum entanglement is often seen as a key metric [10–12]. In the current era of Noisy Intermediate-Scale Quantum (NISQ) devices, researchers have produced ever larger entangled states and improved entanglement measurement strategies, including the demonstration of bipartite entanglement [13, 14], Genuine Multipartite Entanglement (GME) on Greenberger-Horne-Zelinger (GHZ) and cluster states up to 32 [15, 16] and 51 [17] qubits, respectively.

In this work, we go beyond the generation and verification of entanglement and consider the utility of entanglement via the realisation of quantum state teleportation across multiple qubits. Such utilisation of entanglement is an important ingredient in hardware circuit compilation for both qubit pathfinding and implementing long-range gates, which are important elements in creating large-scale entanglement and benchmarking the capabilities of a quantum device. Since Bennett et al.[18] first proposed quantum state teleportation, efforts have been made to physically realise and demonstrate quantum teleportation since two decades ago. The phenomenon of quantum teleportation

was first experimentally verified by [19] in 1997, with teleportation of a polarised state in [20]. In addition, potential applications that use the principle of quantum teleportation have also been discovered, such as dense coding that allows one to communicate two bits of classical information by just sending one bit of classical information [21], quantum encrypted communication [22], and detection of entanglement by teleporting the quantum state through photon modes of an extended Eienstein-Podolsky-Rosen (EPR) state [23]. As time progressed, researchers have successfully performed teleportation onto distant qubits [24, 25]. Lately, there have been breakthroughs in long-range quantum gates based on dynamic measurements that teleport locally connected gates [26, 27] that also share a similar principle as entanglement swapping [28]. However, there still lacks sufficient experimental verification of teleportation on entangled states at a level of a two-digit number of qubit hops.

Here, we implement a teleportation protocol [29] based on single-qubit measurements on entangled graph states. The experiments were conducted on the IBM Quantum device *ibm_sherbrooke* consisting of 127 superconducting transmon qubits [30] using the workflow shown in Figure 1. We characterise and sustain the entanglement of two-qubit graph states that have one of their qubits teleported along the one-dimensional qubit paths up to 19 hops. It is found that a higher level of entanglement can be sustained if the paths used for teleportation are selected based on optimised net negativity, further highlighting the importance of entanglement benchmarking on a quantum device using bipartite negativities [16]. We implement two approaches to teleportation: post-selection and dynamic circuits. Post-selection preserves the form of the teleported two-qubit state by categorising measurements, while dynamic circuits correct the teleported two-qubit state to its original form using mid-circuit measurements. By comparing the robust-

* haiyuek@student.unimelb.edu.au

† john.kam@monash.edu

‡ mooney.g@unimelb.edu.au

§ lloydch@unimelb.edu.au

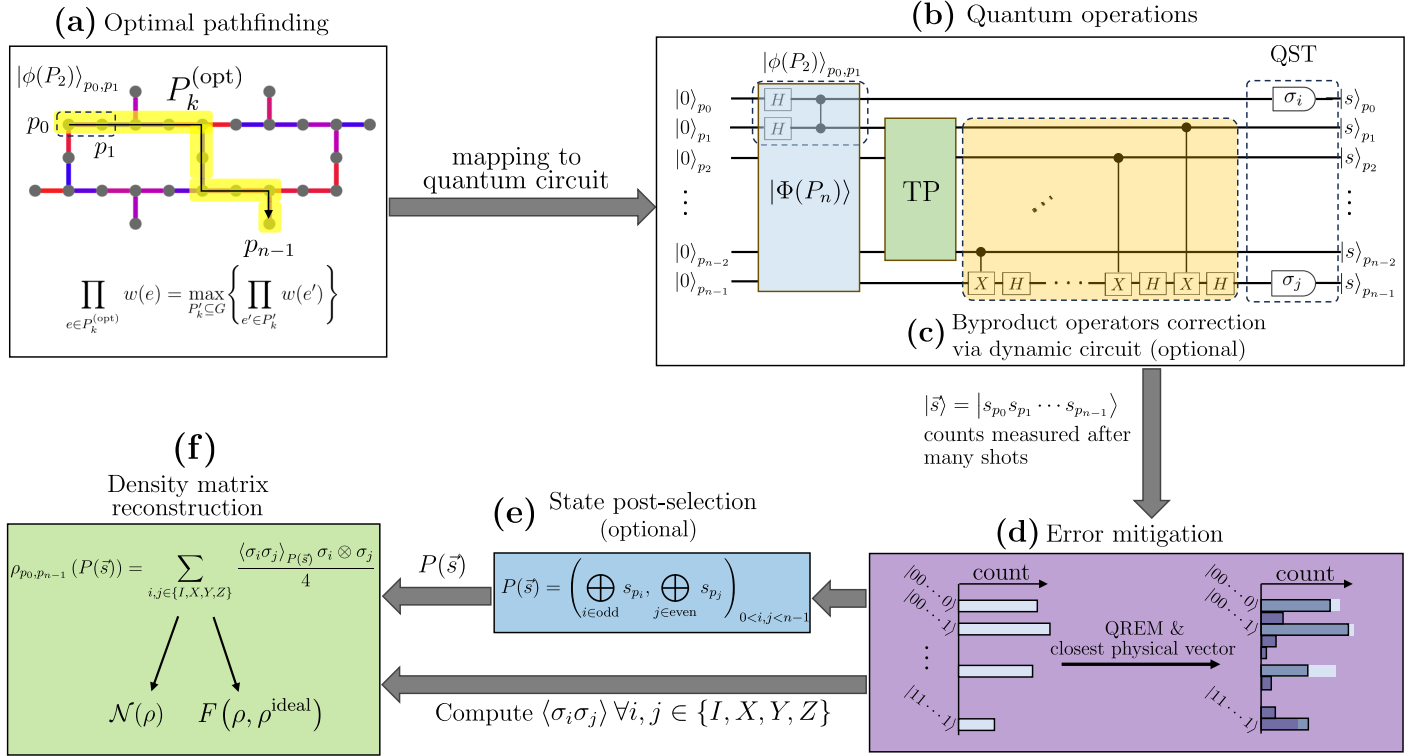


FIG. 1. Overview of the teleportation workflow. **(a)** Optimal pathfinding: as in Section IV, the line of qubits on the quantum device of a given path length k is calculated based on maximising the edge weight product. **(b)** Quantum operations: a one-dimensional graph state is generated on the quantum circuit and the teleportation (TP) of the component of $|\phi(P_2)\rangle$ on p_1 to p_{n-1} is performed through the measurement of intermediate qubits in the Pauli- X basis as described in Section II. At the end, the teleported state is measured in every Pauli basis combination to perform Quantum State Tomography (QST). **(c)** Byproduct operators correction applied via dynamic circuit described in Section V A as a mode of teleportation can be incorporated into the circuit to undo the local transformations acquired in the protocol. **(d)** Error Mitigation: applies Quantum Readout Error Mitigation (QREM) and removes unphysical negative counts that can arise after mitigation, as described in Section III. **(e)** State post-selection described in Section V B as another mode of teleportation used to discriminate the different projected Bell pairs. **(f)** Density matrix reconstruction of the teleported two-qubit state to calculate their corresponding negativity or fidelity.

ness of these strategies with direct state transportation via a sequence of SWAP gates, we find that the post-selection method outperforms the others in terms of the preservation of entanglement.

II. TELEPORTATION ALONG ONE-DIMENSIONAL GRAPH STATES

To prepare for quantum teleportation, one of the necessary prerequisites is the establishment of an entangled state between the teleporter and receiver sites. We generate a pair of entangled qubits and a path of entangled qubits with the intention of teleporting one of the qubits from the pair along the path. The entangled path is prepared as a graph state that comprises the second qubit, subsequent conduit ‘hopping’ qubits, and the final qubit at the end receiver site. In the following, we trace through the

theoretical framework of our setup by initially considering the teleportation of a qubit from an arbitrary two-qubit state. As shown in Figure 2, an arbitrary quantum state $|\phi\rangle_{0,1} = U(|\alpha\rangle \otimes |\beta\rangle)$ is prepared on qubit 0 and 1, and teleported along a path of qubits that are already entangled via Controlled- Z (CZ) gates acting on $|+\rangle$ states. By measuring qubit 1 of the path in the Pauli- X basis, the information on that qubit is teleported to its neighbouring qubit 2 prepared in $|+\rangle$, while acquiring a local transformation depending on the measurement outcome applied to the state. The process can be repeated by measuring qubit 2 and treating the next-neighbouring qubit as the receiver. More importantly, while qubit 1 is being teleported to a target qubit, any form of entanglement previously established with other qubits is preserved. This feature allows us to perform entanglement characterisation over distant qubits by teleporting the state initially prepared on adjacent qubits.

We describe the natural evolution of the quantum state

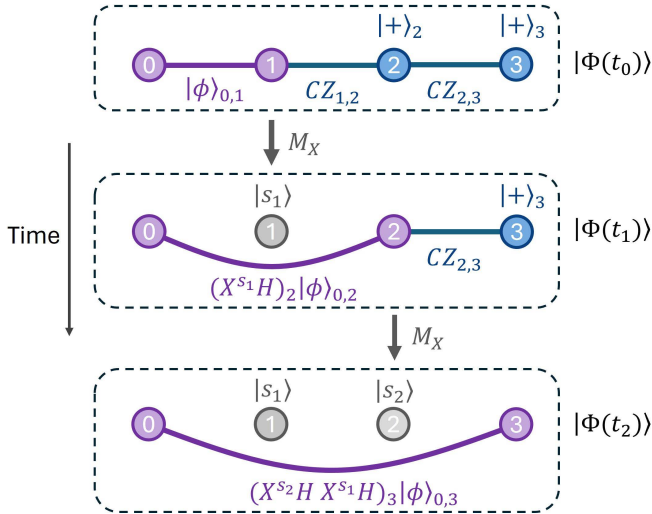


FIG. 2. Demonstration of steps to teleport the component of $|\phi\rangle_{0,1}$ on qubit 1, which is entangled with qubit 0—illustrated in purple—towards the rightmost qubit. First at t_0 , initialise the two-qubit state $|\phi\rangle_{0,1}$ and entangle with Pauli-X basis eigenstates $|+\rangle$ via CZ gates, producing an overall state $|\Phi(t_0)\rangle = CZ_{2,3} CZ_{1,2} |\phi\rangle_{0,1} |+\rangle_2 |+\rangle_3$; Measuring qubit 1 in the Pauli-X basis where $M_{X_1} = M_{1,s_1} H_1$ (see Equation A6 in Appendix A for details), yielding a measurement result of $|s_1\rangle$, where $s_1 = 0$ or 1 , producing the state $|\Phi(t_1)\rangle = |s_1\rangle \otimes CZ_{2,3} (X^{s_1} H)_2 |\phi\rangle_{0,2} |+\rangle_3$; Finally, another measurement on qubit 2 yields result s_2 , leaving the teleported state at t_2 to be the same state as $|\phi\rangle$ up to some local transformations, namely $|\Phi(t_2)\rangle = |s_1 s_2\rangle \otimes (X^{s_2} H X^{s_1} H)_3 |\phi\rangle_{0,3}$. Since the local transformations are known after measurements, they can be used to retrieve the original state $|\phi\rangle_{0,3}$ now defined over qubits 0 and 3. This procedure can be generalised to teleport the qubit 1 of the original entangled state across a path with an arbitrary number of nodes connected by CZ gates.

for the measurement-based teleportation protocol as follows (see Appendix A for details). In the Appendix, we derive the following results: Let $|\phi\rangle_{0,1}$ be an arbitrary two-qubit state prepared on qubits 0 and 1 that is entangled with—using a CZ gate—a path graph state of $n-2$ qubits to produce a state with the form:

$$|\Phi\rangle = \left(\prod_{i=1}^{n-2} CZ_{i,i+1} \right) \bigotimes_{j=2}^{n-1} |+\rangle_j \otimes |\phi\rangle_{0,1} \quad (1)$$

By measuring all intermediate qubits from label 1 to $n-2$ in the X -basis with outcome $\vec{s} = (s_1, s_2, \dots, s_{n-2})^T$, the qubit 1 component of state $|\phi\rangle_{0,1}$ is teleported along the path to qubit $n-1$ to produce $|\phi\rangle_{0,n-1}$, while acquiring some local transformations depending on the measured results \vec{s} , which arrives at $|\Phi\rangle^{(\text{Teleported})} = \left(\prod_{i=1}^{n-2} X_{n-1}^{s_i} H_{n-1} \right) |\phi\rangle_{0,n-1} \otimes |\vec{s}\rangle$ that agrees with the result in [29].

Next, we begin the description from the general definition

of a graph state. According to the construction, a graph state mapped from a graph $G = (V, E)$ with vertices set V and edge set E corresponding to two-qubit connections, is defined as

$$|G\rangle := \prod_{(i,j) \in E} CZ_{i,j} |+\rangle^{\otimes n}, \quad (2)$$

where $n = |V|$ is the number of qubits, and $CZ_{i,j}$ is the controlled- Z gate acting on edge (i, j) of the graph G . We can set up the two-qubit state $|\phi\rangle_{0,1}$ to be teleported as a simple graph state on path P_2 with two vertices and an edge connecting them,

$$|\phi\rangle_{0,1} = \frac{1}{2}(|00\rangle + |01\rangle + |10\rangle - |11\rangle)_{0,1} := |\phi(P_2)\rangle_{0,1}. \quad (3)$$

The prepared n -qubit state (where $n > 2$) for the teleportation procedure $|\Phi\rangle$ is thus $|\phi\rangle_{0,1}$ entangled with an end qubit of a path graph state of $n-2$ qubits via a CZ gate, resulting in a path graph state defined on the path graph P_n . The explicit form of this path graph state on P_n with vertices $V(P_n) = \{0, 1, \dots, n-1\}$, and edges $E(P_n) = \{(0, 1), (1, 2), \dots, (n-2, n-1)\}$ can be obtained as

$$|\Phi(P_n)\rangle = \frac{1}{\sqrt{2^n}} \sum_{\vec{x} \in \{0,1\}^{\otimes n}} \prod_{i=0}^{n-2} e^{i\pi x_i x_{i+1}} |\vec{x}\rangle. \quad (4)$$

where $|\vec{x}\rangle = |x_0, x_1, \dots, x_{n-1}\rangle$, and x_i is the i^{th} binary value in \vec{x} . The product of $e^{i\pi x_i x_{i+1}}$ is the phase picked up from every component $|\vec{x}\rangle$ after applying CZ gate to all nearest-neighbour qubits.

From Result A2, the teleported two-qubit graph state acquires local transformations in the following form

$$|\psi\rangle_{0,n-1}^{(\vec{s},n)} := (X^{s_{n-2}} H \dots X^{s_2} H X^{s_1} H)_{n-1} |\phi(P_2)\rangle_{0,n-1}, \quad (5)$$

where H, X are the Hadamard and Pauli X gates respectively. At a given number of intermediate qubits $n-2$, the teleportation produces exactly a total of four configurations of local transformations on $|\phi(P_2)\rangle_{0,n-1}$ depending on the measurement results \vec{s} . Hence, using the identities $H^2 = I$, $H X^{s_i} H = Z^{s_i}$ and ignoring global phase induced when swapping the order of X and Z , we can manipulate Equation 5 to obtain

$$\begin{aligned} |\psi\rangle_{0,n-1}^{(\vec{s},n)} &= I_0 \otimes (H^n Z^{s_1 \oplus s_3 \oplus \dots \oplus s_{n-2}} X^{s_2 \oplus s_4 \oplus \dots})_{n-1} |\phi(P_2)\rangle_{0,n-1} \\ &:= |\phi(P_2)\rangle_{0,n-1}^{(\vec{s},n)}, \end{aligned} \quad (6)$$

where the symbol \oplus denotes binary addition (XOR). No matter how long the path is, the teleported state $|\psi\rangle_{0,n-1}^{(\vec{s},n)} =$

$|\phi(P_2)\rangle_{0,n-1}^{(\vec{s},n)}$ always falls into one of the four configurations, and we can distinguish them by evaluating the discriminator inspired from [31],

$$P(\vec{s}) = \left(\bigoplus_{i \in \text{odd}} s_i, \bigoplus_{j \in \text{even}} s_j \right). \quad (7)$$

As a function of \vec{s} , the discriminator evaluates the powers of X and Z in Equation 6 and the output for each is either 0 or 1. Therefore, there are precisely four possible outcomes of $P(\vec{s})$, each categorising one configuration of local transformation.

III. MEASURES OF TELEPORTATION SUCCESS

To determine the success of teleportation, we consider two properties in our experiments: negativity and fidelity.

A. Negativity

To quantify the amount of entanglement between two qubits of the teleported graph state as a Bell state up to local transformation in Equation 6, we employ an entanglement measure by calculating the negativity of the reduced density matrix of qubit 0 and qubit $n - 1$ [32]. For a given density matrix ρ of a quantum system, its negativity $\mathcal{N}(\rho)$ with respect to fixed bipartitions a and b is given by

$$\mathcal{N}(\rho) = \frac{1}{2} (\|\rho^{T_a}\| - 1) = \left| \sum_{\lambda_i < 0} \lambda_i \right|, \quad (8)$$

where λ_i are the negative eigenvalues of the partial transpose ρ^{T_a} with respect to partition a [33]. In our case, $a = 0$ and $b = n - 1$. The negativity has a value between 0 and 0.5, i.e. $0 \leq \mathcal{N} \leq 0.5$, and the higher the value implies more entanglement. N.B. for two qubits, non-zero negativity is a necessary and sufficient condition for entanglement [14].

To reconstruct the density matrix ρ , we perform full Quantum State Tomography (QST) on the resulting two-qubit state [34]. The sampled probabilities for measurement in each two-qubit Pauli bases are calibrated with Quantum Readout Error Mitigation (QREM) [35] to adjust for classical errors introduced during the qubit readout process. However, instead of calibrating all qubit readouts simultaneously, we correct the probability vector qubit-wisely [36] such that the dimension of the calibration matrices only needs to be 2×2 for each iteration. Unphysical negative probabilities can arise due to shot noise and device drift between the QREM calibration and the experiment. These are addressed using the Michelot algorithm to efficiently find the closest probability vector [37]. The constructed

density matrix could contain unphysical negative eigenvalues caused by noise in the quantum computation. We use the efficient algorithm by Smolin et al. to find the nearest physical density matrix [38].

B. Fidelity

The fidelity of a measured state is its overlap with the expected ideal state, making it a natural measure for the success of teleportation. The fidelity F of any prepared (noisy) state ρ with respect to its ideal target state ρ^{ideal} is defined as

$$F(\rho, \rho^{\text{ideal}}) = \text{tr}(\rho \rho^{\text{ideal}}). \quad (9)$$

In the teleportation protocols, the state ρ , is the teleported 2-qubit graph state. It's density matrix is constructed using QST in the same manner as for measuring the negativity with QREM applied.

IV. TELEPORTATION PATH OPTIMISATION

We propose three pathfinding protocols to maximise the amount of entanglement preserved after teleportation and the number of intermediate qubits that the state $|\phi\rangle$ can teleport across while maintaining entanglement, certified by non-zero negativity [32]. These protocols select the optimal path for teleportation from the quantum device based on the nearest-neighbour qubit-pair properties: entanglement negativity, negativity with quantum readout error mitigation (QREM), and two-qubit gate error. For a quantum device, we first construct an entanglement (or fidelity) graph G where the vertices $V(G)$ represent all qubits and edges $E(G)$ represent the available couplings between them with weights assigned as the two-qubit negativity (or fidelity). The optimal n -qubit path $P_n^{(\text{opt})} \subseteq G$ used for teleportation is chosen to satisfy the following condition

$$\prod_{e_{ij} \in E(P_n^{(\text{opt})})} w(e_{ij}) = \max_{P'_n \subseteq G} \left\{ \prod_{e'_{ij} \in E(P'_n)} w(e'_{ij}) \right\}, \quad (10)$$

where P'_n is any path subgraph of G with length $n - 1$ and $w(e_{ij})$ is the weight of edge e_{ij} assigned based on the pathfinding protocol. In the experiments, we select the best four paths (including $P_n^{(\text{opt})}$) based on the ordering of edge weight products using Algorithm B1.

In the first protocol, we determine the optimal path $P_n^{(\text{neg graph opt})}$ at a given path length using the edge weight assignment $w(e_{ij}) = 2\mathcal{N}(\rho_{i,j}^{\text{Bell}})$, where $\mathcal{N}(\rho_{i,j}^{\text{Bell}})$ is the average negativity of the Bell states projected from the native graph state prepared on the whole device to the incident qubits i, j via neighbouring qubit Z -basis projections [16]. The reason that the negativity is doubled is to expand the

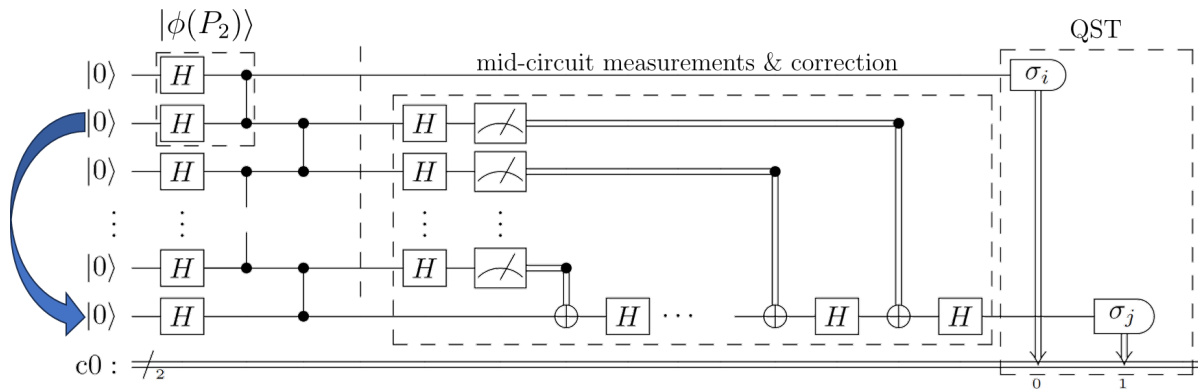


FIG. 3. Illustration of the dynamic circuit approach to quantum teleportation. Initially, a graph state of n qubits along the path $|\phi(P_n)\rangle$ is generated. The intermediate qubits are measured in the Pauli- X basis by applying a Hadamard gate before measuring in the computational Pauli- Z basis. According to the measurement results, a sequence of X and Hadamard gates are conditionally applied to the last qubit to undo the local transformation. At this stage, the two qubits of the two-qubit graph state $|\phi(P_2)\rangle$ are now separated to the ends, as indicated by the blue arrow, making the overall quantum state in the ideal case equal to $|\phi(P_2)\rangle \otimes |s_1 s_2 \cdots s_{n-2}\rangle$. Finally, Quantum State Tomography is performed to obtain the teleported two-qubit density matrix ρ by measuring the first and last qubits in all combinations of Pauli bases. The double line at the bottom represents classical registers storing measurement results.

edge weights to the range of $[0, 1]$ so that $w(e_{ij}) = 1$ indicates maximal entanglement.

In the second pathfinding protocol, we determine the optimal path $P_n^{(\text{neg QREM graph opt})}$ using the same assignment of edge weights as for selecting the optimal path $P_n^{(\text{neg graph opt})}$, except that $\mathcal{N}(\rho_{i,j}^{\text{Bell}})$ are measured using QREM.

In the third protocol, the optimal path $P_n^{(\text{gate fid graph opt})}$ is chosen by assigning the edge weights to be the two-qubit gate fidelities determined from the IBM Quantum device gate-error map, using the expression

$$w(e_{ij}) = 2 \left(\frac{1}{2} - \epsilon_{ij} \right), \quad (11)$$

where $\epsilon_{ij} \in [0, 1/2]$ is the two-qubit gate error rate between qubits i and j . Sometimes error rates calculated during IBM Quantum device calibrations are undefined and consequently displayed as a value of 1. Since error rates above 0.5 have no practical significance, they are excluded from the candidates of optimal paths. In our experiment, only 4 edges out of 144 are excluded, which has little effect on our choice of optimal path.

V. RESULTS

Following the procedures on path optimisation, teleportation and entanglement measurement summarised in Figure 1, we describe and implement two approaches to teleportation on the IBM Quantum *ibm_sherbrooke* device in Section V A and Section V B respectively. We examine

their performance using each of the path optimisation procedures, with and without QREM applied to the teleportation measurements. Additionally, the performance of the teleportation protocols is compared with direct state teleportation using SWAP gates in Section V C. The source code and datasets generated for this program are available under the GitHub repository [39].

A. Dynamic circuit approach to teleportation

We perform the measurement-based teleportation protocol using the IBM Quantum dynamical circuits capability. Similarly to the principle behind the entanglement swapping [28], mid-circuit measurements are performed on entangled states followed by byproduct correction operators. Since measurement gates are inserted into the middle of a quantum circuit, this results in a collapse of the quantum state that is not recoverable by applying a set of Hermitian conjugate gates [40]. However, this also enables dynamic modification of the circuit during execution by directly measuring some of its qubits and conditionally applying gates to the rest of the circuit based on the outcomes. We note that one-way quantum computation can be performed on IBM Quantum devices through the use of dynamic circuits [23, 27]. In this subsection, we will discuss the use of byproduct operators for correction after mid-circuit measurement within the teleportation procedure.

Using the procedure outlined in Section II, we first design the circuits with dynamical modifications to measure the negativities of the two-qubit graph states after teleportation. As in Figure 3, we prepare the graph state on a path of n vertices and measure intermediate qubits in the

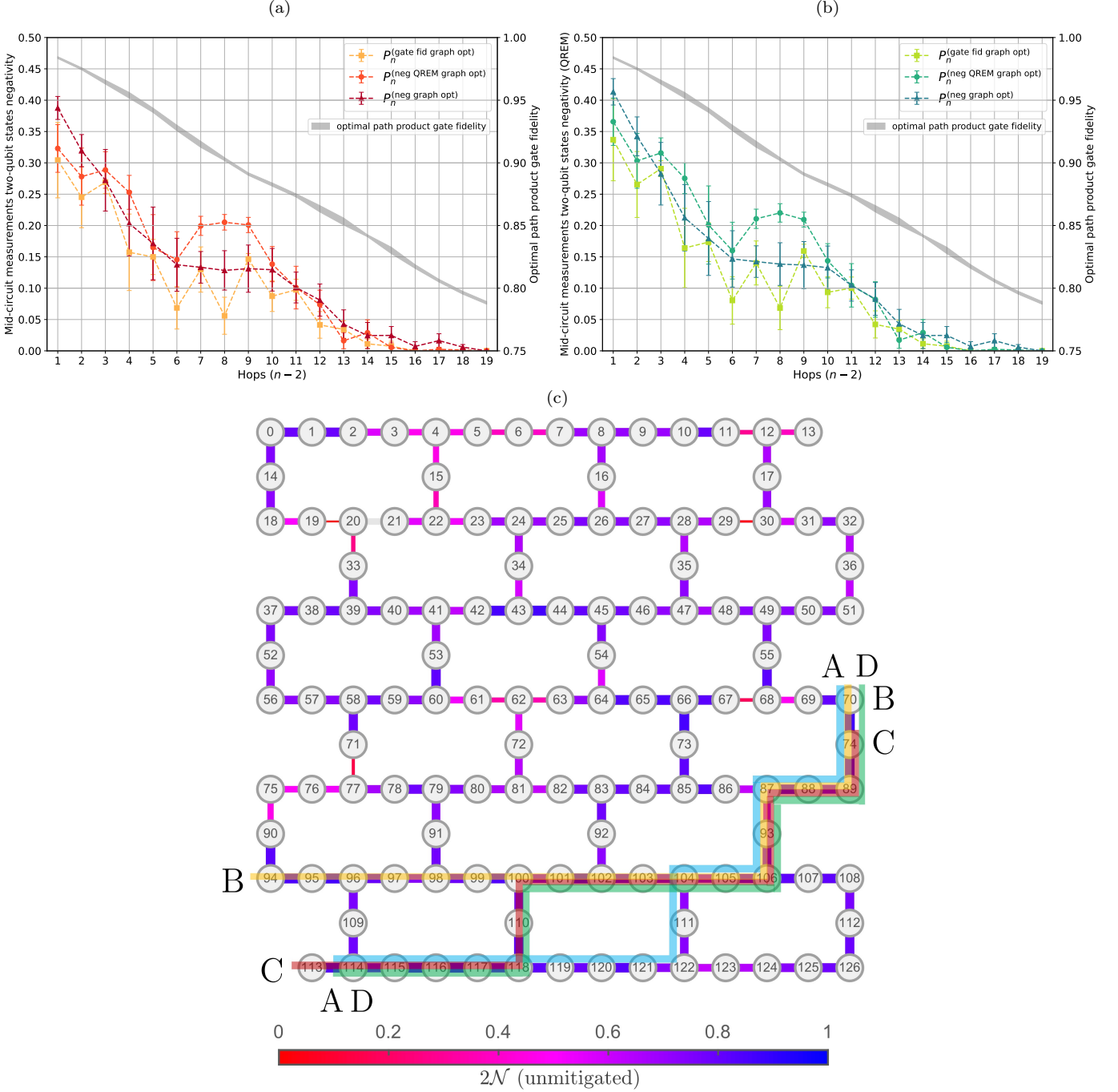


FIG. 4. Graphics showing results for the dynamic circuit approach to teleportation on optimal paths selected from the *ibm_sherbrooke* device. **(a)** The negativity without QREM measured on final two-qubit states against the number of qubits hops in teleportation. **(b)** The negativity with QREM measured on final two-qubit states against the number of qubit hops in teleportation. Due to controlled quantum operations after measuring intermediate qubits, QREM is naturally only applied to the two qubits. Both **(a)** and **(b)** also show the products of two-qubit gate fidelities in $\{P_n^{(\text{gate fid graph opt})}\}$ on the second vertical axis as a point of reference. The different optimal path protocols used are represented by distinct colours on the plot, where each data point has its negativity averaged over the best four paths at the given number of hops and each path is sampled in four trials. Error bars use two times the standard error of the sampled negativities. **(c)** The four paths found with the highest net product of nearest-neighbour negativity $\{P_{19}^{(\text{neg graph opt})}\}$ as described in Section IV that have a path length of 18 (17 intermediate qubits). The paths are drawn on top of the coupling map, where each node represents a qubit and coloured edges represent the available nearest-neighbour couplings with weights $w(e_{ij}) = 2\mathcal{N}_{ij}$, where \mathcal{N}_{ij} is the negativity measured between qubits i and j . Each path is displayed with a distinct colour, and its ends are marked by the same letter: A, B, C, D.

Pauli- X basis by applying a Hadamard gate before measuring in the computational Pauli- Z basis. To recover the form of the initial two-qubit graph state, $|\phi(P_2)\rangle$, dynamical circuits are used to apply byproduct operators on the teleported two-qubit state, where a set of conditional Pauli- X and Hadamard gates are sequentially acted on the last qubit. The purpose of implementing byproduct operators after mid-circuit measurements is to undo any variations of the state caused by projections from measured intermediate qubits. Ideally, the sequence of gates can be simplified to a maximum of two sequential Clifford gates using the discriminant vector shown in Equation 7, ensuring the number of quantum gates involved in the correction remains constant with respect to the number of qubits. However, the IBM Quantum devices do not currently support a classical XOR operation acting on the classical register required for the simplification. Thus, all byproduct operators are applied sequentially. Note that during the application of byproduct operators, instead of applying quantum CNOT gates to the last qubit controlled on post-measured qubits, IBM Quantum devices actively apply quantum X gates based on the mid-circuit measurement results. The classical layer of processing involved in dynamic circuits includes latency overhead that limits the readout and write speeds.

In Figure 4, we present the results for the dynamic circuit approach to teleportation on optimal paths selected from the *ibm_sherbrooke* device. Figure 4a and 4b show the negativity of the final two-qubit state against the number of qubit hops in teleportation for the cases of no QREM and QREM respectively. Negativity is derived from the density matrix of the two-qubit graph state teleported along optimal paths found using the protocols outlined in Section IV with varying numbers of intermediate qubits. As we increment the number of teleportation hops, the average measured negativity of the final teleported state decreases. In our experiment, employing the mid-circuit measurement protocol, the maximal number of teleportations yielding reliable non-zero negativity is 17, with the best four paths $\{P_{19}^{(\text{neg graph opt})}\}$ shown in Figure 4c. However, due to the dynamic corrections to the teleported state, most qubits remain idle during classical processing. This leads to a rapid overall decrease in negativity caused by decoherence and free rotations [16], significantly impacting the level of entanglement during teleportation. Another observation is that regardless of whether QREM is applied, the data show an improvement in teleported entanglement on average, although modest, when states are teleported along the paths $\{P_n^{(\text{neg graph opt})}\}$ and $\{P_n^{(\text{neg QREM graph opt})}\}$ compared to $\{P_n^{(\text{gate fid graph opt})}\}$. These results indicate an advantage in using the negativity map over the gate error map for finding optimal paths, highlighting its potential in general quantum circuit compilation.

Additionally, there appears to be a considerable improvement for paths with 3 to 9 qubit hops when chosen from $\{P_n^{(\text{neg QREM graph opt})}\}$. This behaviour is likely due to the

two methods of measuring negativities weighting sources of noise differently. In particular, decoherence and 2-qubit free rotations [16] are likely to be more emphasised when choosing optimal paths if QREM is applied. Since dynamical circuits involve long idle times for classical processing, this emphasis on non-readout related errors achieved with QREM could be beneficial. Longer paths naturally have higher levels of readout error. Thus, the performance of paths chosen without QREM $\{P_n^{(\text{neg graph opt})}\}$, which put more weight on readout errors, would be expected to improve over $\{P_n^{(\text{neg QREM graph opt})}\}$. This could explain their slight advantage for paths with 15 or more hops. In the next subsection, we investigate post-selection based teleportation, which circumvents the long idle times involved in the classical processing of mid-circuit measurements.

B. Post-Selected approach to teleportation

Similar to the mid-circuit measurements based teleportation, we also employ X -basis measurements to project the two-qubit graph state. However, instead of inserting quantum gates dynamically after measurements, we categorise the teleported state into one of the four possible configurations using the discriminator shown in Equation 7 on the measurement outcomes of intermediate qubits. This approach aims to tackle the problem of errors arising due to idling qubits during mid-circuit measurements by reducing the circuit depth and shifting measurements to the end of the circuits. Figure 5 outlines the modified algorithm. By recording the measurement outcomes of the intermediate qubits, we identify the teleported state configuration after the circuit is completed. Since the resulting two-qubit state can be categorised directly by Equation 7, there is no need to apply byproduct operators, and the entanglement for each category can be calculated independently. Therefore, the depth of the quantum circuit is reduced and the mid-circuit measurements are no longer needed. This largely avoids errors caused by decoherence and free rotations, establishing a cleaner environment for benchmarking the loss of information caused by gate noise during teleportation. It also enables us to apply QREM on the full path of qubits. However, unlike the correction after mid-circuit measurements, this method would project the teleported state into one of the four variants randomly at a fixed number of intermediate qubits previously stated in Section II. Reconstructing the density matrix $\rho = |\phi(P_2)\rangle \langle \phi(P_2)|$ directly would obtain a mixed state,

$$\rho^{(\text{mixed})} = \frac{1}{2^{n-2}} \sum_{\vec{s}} |\phi(P_2)\rangle^{(\vec{s},n)} \langle \phi(P_2)|^{(\vec{s},n)}. \quad (12)$$

Instead, the measurement outcomes are categorised into the four possible Bell state/two-qubit graph state configurations before calculating their corresponding density matrices $\rho^{(\vec{s},n)}$. Since the categorisation can be easily de-

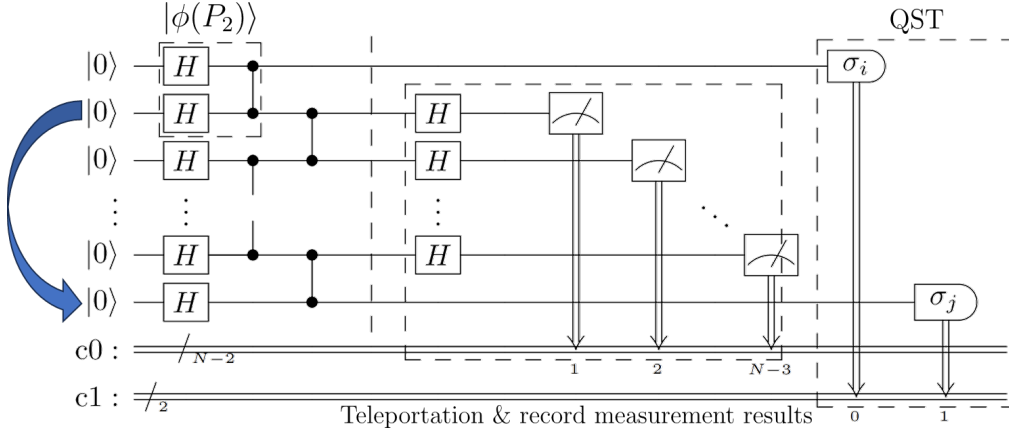


FIG. 5. Illustration of the teleportation circuit based on post-selection. The key distinction from the protocol outlined in Figure 3 lies in the absence of conditional modifications during circuit execution. Instead, we categorise the projected state through classical post-selection. Thus, the exact local transformations on the teleported two-qubit graph state are identified according to the measurement outcomes stored in the classical register $c0$ for each shot. If ignoring the measurement results of intermediate qubits, the system exists in an overall mixed state with pure state components of $|\phi(P_2)\rangle^{(s,n)} \otimes |s_1 s_2 \dots s_{n-2}\rangle$ before QST.

terminated from the discriminant vector as shown in Equation 7, the process of undoing local transformations $S = (X^{s'_{n-2}} H) \dots (X^{s'_2} H)(X^{s'_1} H)$ by computing $\rho = S^\dagger \rho' S$ is not necessary.

Figure 6a and Figure 6b show the average negativities measured from each of the four configurations on *ibm_sherbrooke* as a function of the number of hops teleported in light-coloured lines. The mean negativities averaged over four configurations are shown in dark-coloured lines. Similar to results from Figure 4a, 4b, the two-qubit graph state is teleported along the same optimal paths using the same protocols. We also observe the negativity decreases as the number of qubits hopped during teleportation increases, indicating non-perfect teleportations due to noise, as well as the improvement in the measured negativity after applying qubit-wise QREM. However, on average the negativity preserves better compared to the approach using mid-circuit measurements. Even after hopping 19 qubits, the entanglement of the teleported state recognised by post-selection still maintains significant non-zero negativity, whereas the negativities measured from the mid-circuit measurement approach all drop to zero. Specifically, the mitigated negativity of the states teleported along the best four paths $\{P_{21}^{(\text{neg graph opt})}\}$ (as shown in Figure 6c) has an average reading of 0.108. This strongly demonstrates the advantage of post-selection in preserving entanglement during teleportation by reducing circuit depth and shifting measurements to the end. We anticipate that the highest number of teleportation hops is not limited to 19, suggesting a direction in future research of adding more hops to teleportation until the extreme is reached.

Compared to the results from mid-circuit measurement experiments, it is more evident that, on average the entanglement of the states teleported along

$\{P_n^{(\text{neg graph opt})}\}$ paths preserve more entanglement than $\{P_n^{(\text{gate fid graph opt})}\}$ both in Figure 6a and Figure 6b. Additionally, more qubits are teleported across while the negativity remains non-zero (19 in $\{P_n^{(\text{neg graph opt})}\}$ versus 18 in $\{P_n^{(\text{gate fid graph opt})}\}$). This further highlights the importance of entanglement benchmarking using nearest-neighbour negativity [16], as a better indicator of optimal paths. However, as the number of intermediate qubits increases, despite the considerable amount of improvement in the measured negativity compared to Figure 6a, we still find that the results from $\{P_n^{(\text{neg QREM graph opt})}\}$ paths underperform the results from $\{P_n^{(\text{neg graph opt})}\}$ paths for larger number of hops in Figure 6b, which also happens consistently in Figure 4b. This is likely due to the negativities calculated without QREM putting more weight on readout errors compared to with QREM, since longer chains become more dominated by readout errors, making negativity without QREM a better indicator for path optimisation. We also suspect that $\{P_n^{(\text{neg QREM graph opt})}\}$ could actually put more weight on qubits that benefit more from QREM, leading to QREM being more likely to be effective on the teleportation protocol as well. This could be investigated in future work.

C. Comparisons with SWAP gates approach

In previous subsections, we have shown that the entanglement decays as the number of hops in teleportation grows. We also comment on the performance of post-selected categorisation that surpasses the performance of the mid-circuit measurement approach. In this subsection, we investigate SWAP gates as a reference method for transporting the

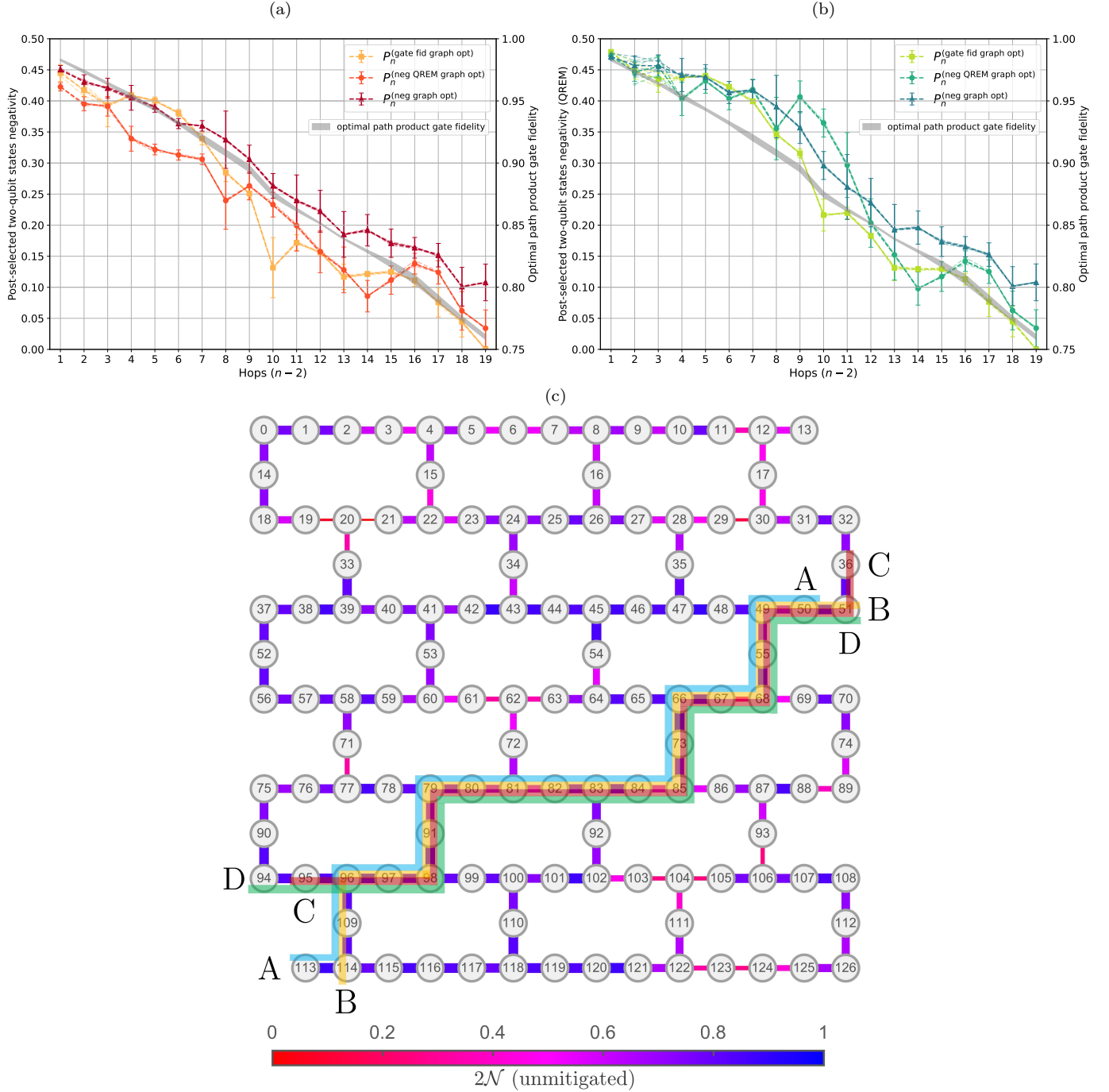


FIG. 6. Graphics showing results for the post-selected approach to teleportation on optimal paths selected from the *ibm_sherbrooke* device. **(a)** The negativity without QREM measured on final two-qubit states against the number of qubits hops in teleportation. **(b)** The negativity with qubit-wisely applied QREM measured on final two-qubit states against the number of qubits hops in teleportation. Both **(a)** and **(b)** show the products of two-qubit gate fidelity on $\{P_n^{(\text{gate fid graph opt})}\}$ on the second vertical axis as a point of reference. The different optimal path protocols used are represented by distinct colours on the plot, where each data point has its negativity averaged over the best four paths at the given number of hops and each path is also sampled in four trials. Different from Figure 4, there are also light-coloured dashed lines to distinguish the results among four configurations. N.B. that only two configurations are available when there is just one hop, and the remaining two are omitted in the plot. Error bars represent two times the standard error of the sampled negativities. **(c)** The four paths found with the highest net product of nearest-neighbour negativity $\{P_{21}^{(\text{neg graph opt})}\}$ described in Section IV with a path length of 20 (19 intermediate qubits). The paths are drawn on top of the negativity coupling map of the quantum device *ibm_sherbrooke*, where each node represents a qubit and coloured edges represent the available nearest-neighbour couplings with weights $w(e_{ij}) = 2\mathcal{N}_{ij}$, where \mathcal{N}_{ij} is the negativity measured between qubits i and j . Each path is displayed with a distinct colour, and its ends are marked by the same letter: A, B, C, D.

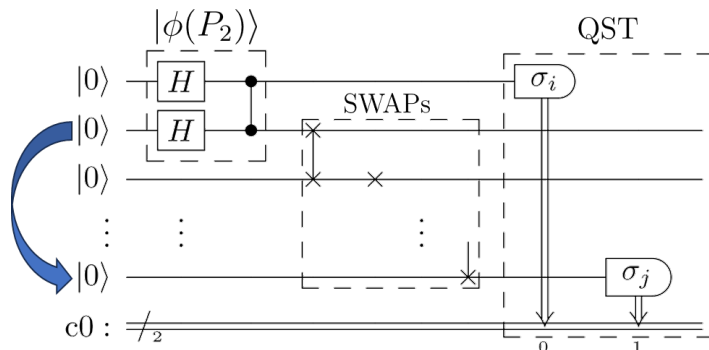


FIG. 7. Circuit diagram of the simple and naive design to transport the information of the second qubit to the last by continually applying SWAP gates. Ideally, the quantum state before QST should be in the form of $|\phi(P_2)\rangle_{0,n-1} \otimes |00 \dots 0\rangle$.

state from the second qubit to the last, as illustrated in Figure 7, where

$$\text{SWAP}_{01} |\alpha\rangle_0 \otimes |\beta\rangle_1 = |\beta\rangle_0 \otimes |\alpha\rangle_1 \quad (13)$$

simply swaps the quantum states between two qubits on the computational basis. We also compare the entanglement measured across all discussed approaches in Figure 8, emphasising the improvement achieved in post-selected categorisation.

In Figure 8a, we plot the mitigated negativity averaged over all three protocols of optimal paths against the number of hops for both teleportation schemes and the results obtained using SWAP gates. Overall, the entanglement of the state teleported with post-selected categorisation consistently preserves better, even after considering all of the negativity measured regardless of the choice of paths as shown in the shaded region. This highlights the advantage of the post-selection method in reducing circuit depth and decoherence of idling qubits during dynamic operations. We also notice that on average, the post-selected categorisation method achieves the longest teleportation distance of 19 hops before the final negativity drops to zero, compared to the other methods that are capped at 17 hops. The faster reduction of entanglement in the graph states using SWAP gates is likely due to the large circuit depth that grows linearly with respect to the number of hops and contributes three CNOTs for every SWAP gate. In contrast, while preserving a relatively high amount of entanglement, the classical post-selected categorisation after teleportation does not rely on additional quantum gates to transmit messages like SWAP gates or byproduct operators.

To reinforce the results in Figure 8a that compare the quality of entanglement using negativity, we also characterise the same teleported states using fidelity as described in Section III, which tells us the overlap between a noisy and ideal state. In Figure 8b, we observe similar behaviour of the teleported state as in Figure 8a, including an overall trend of decaying fidelity as the number of teleportation hops increase, as well as significantly higher reading of the

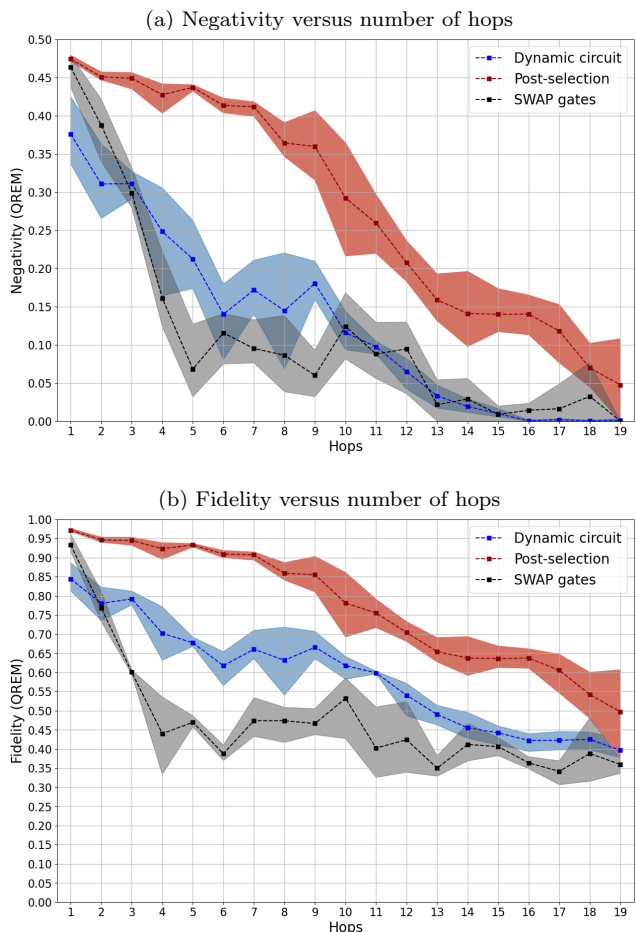


FIG. 8. Plots that compare the performance between the two teleportation protocols and the SWAP gate approach. **(a)** QREM mitigated negativity measured using dynamic circuit, post-selected categorisation, and SWAP gates are plotted together. The shaded region represents the range of negativity measured using different path-optimising protocols; heavy dashed lines are highlighted for their means. **(b)** Same comparison on correction after mid-circuit measurements, post-selected local transformations, and SWAP gates, but using fidelity.

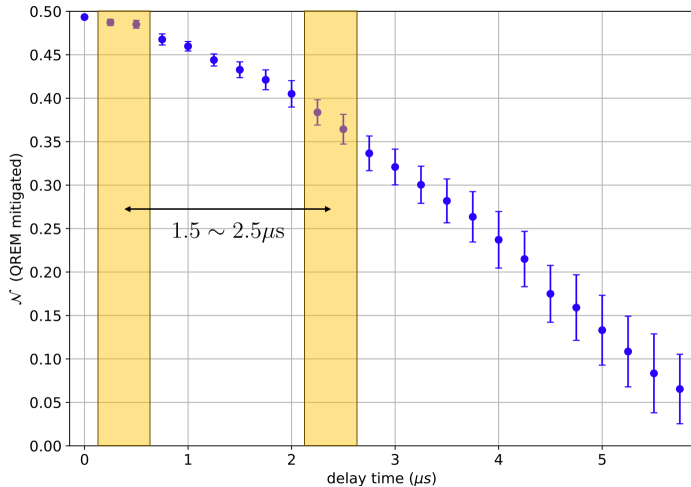


FIG. 9. Plot of the average two-qubit graph state QREM mitigated negativity versus delay time on the IBM Quantum device *ibm_sherbrooke*. The average time for the negativity to decay from near 0.474 (teleportation by once using post-selected categorisation with QREM, marked by the first band) to near 0.376 (teleportation by one hop using mid-circuit measurement with QREM, marked by the second band) is roughly 1.6 μ s to 2.5 μ s.

fidelity from post-selection method. Overall, the results indicate that we have preserved the entanglement of two-qubit states after teleporting them across at least 19 qubits, which benchmarks a high level of performance on IBM Quantum computers in quantum state teleportation.

In addition, we observe on average a considerable gap of 0.098 in the negativity between correction after mid-circuit measurement and the post-selected categorisation method even after just one hop. Yet the circuit’s depth after applying the corrections is only increased by at most two. We attribute this to the long gate execution time of the dynamic CNOT gate, such that there is a significant delay in the circuit within just one hop. To quantify the delay, we measure the average negativity of the two-qubit graph state simply idling on the same machine in Figure 9. The time it takes for the negativity to reduce by the amount indicated above (from 0.474 to 0.376) is roughly 1.5-2.5 μ s. Supposing that this is the effective gate time of the dynamical equivalent to a CNOT gate, it is indeed much longer than the

typical two-qubit gate time on *ibm_sherbrooke*, which has the mean of 533 ns.

VI. DISCUSSION

In this paper, we have demonstrated the teleportation of two-qubit graph states along the path of entangled qubits on physical quantum computers. For comparison purposes, two protocols were used: strict teleportation using a dynamic circuit, and a version based on post-selection. These were compared directly with direct SWAP-based transportation. The results showed the method of post-selected categorisation outperformed the others in terms of minimising information lost during teleportation hops. Under this approach, we sustained the original state entanglement after teleporting 19 hops. We also compared the performance of different optimal pathfinding protocols. In the scenario where the method of post-selected categorisation is carried out, we found that the path that maximises the product of negativities between nearest neighbours sustained entanglement the most, which reflects the utility of entanglement benchmarking using the nearest-neighbour negativity as opposed to the gate error map.

This work provides experimentally verified tools to realise more advanced circuit compilation applications in future research. These include qubit pathfinding and the implementation of high-fidelity long-range gates that do not rely on SWAP gates, which are also important elements in creating large-scale entangled states and benchmarking the capabilities of quantum devices. Furthermore, the results potentially offer a scalable method of measuring entanglement on large, one-dimensional graph states.

Acknowledgments

This work was supported by the University of Melbourne through the establishment of an IBM Quantum Network Hub at the University.

Data Availability Statement

The source code and datasets generated and / or analysed during the current study are available from the corresponding author upon reasonable request.

-
- [1] P. Shor, Algorithms for quantum computation: discrete logarithms and factoring, in *Proceedings 35th Annual Symposium on Foundations of Computer Science* (1994) pp. 124–134.
- [2] L. K. Grover, A fast quantum mechanical algorithm for database search, in *Proceedings of the twenty-eighth annual ACM symposium on Theory of computing* (1996) pp. 212–219.
- [3] A. Peruzzo, J. McClean, P. Shadbolt, M.-H. Yung, X.-Q. Zhou, P. J. Love, A. Aspuru-Guzik, and J. L. O’Brien, A variational eigenvalue solver on a photonic quantum processor, *Nature Communications* **5**, 4213 (2014).
- [4] E. Farhi, J. Goldstone, and S. Gutmann, A quantum approximate optimization algorithm, arXiv preprint arXiv:1411.4028 (2014).
- [5] J. Biamonte, P. Wittek, N. Pancotti, P. Rebentrost,

- N. Wiebe, and S. Lloyd, Quantum machine learning, *Nature* **549**, 195 (2017).
- [6] M. Schuld, I. Sinayskiy, and F. Petruccione, An introduction to quantum machine learning, *Contemporary Physics* **56**, 172 (2014).
- [7] S. McArdle, S. Endo, A. Aspuru-Guzik, S. C. Benjamin, and X. Yuan, Quantum computational chemistry, *Reviews of Modern Physics* **92**, 015003 (2020).
- [8] L. C. L. Hollenberg, Fast quantum search algorithms in protein sequence comparisons: quantum bioinformatics, *Physical Review E* **62**, 7532 (2000).
- [9] R. Orús, S. Mugel, and E. Lizaso, Quantum computing for finance: Overview and prospects, *Reviews in Physics* **4**, 100028 (2019).
- [10] G. Vidal, Efficient classical simulation of slightly entangled quantum computations, *Physical review letters* **91**, 147902 (2003).
- [11] F. Verstraete and J. I. Cirac, Renormalization algorithms for quantum-many body systems in two and higher dimensions, arXiv (2004), cond-mat/0407066 [cond-mat.str-el].
- [12] F. Verstraete, V. Murg, and J. I. Cirac, Matrix product states, projected entangled pair states, and variational renormalization group methods for quantum spin systems, *Advances in physics* **57**, 143 (2008).
- [13] G. J. Mooney, C. D. Hill, and L. C. L. Hollenberg, Entanglement in a 20-qubit superconducting quantum computer, *Scientific Reports* **9**, 10.1038/s41598-019-49805-7 (2019).
- [14] G. J. Mooney, G. A. L. White, C. D. Hill, and L. C. L. Hollenberg, Whole-device entanglement in a 65-qubit superconducting quantum computer, *Advanced Quantum Technologies* **4**, 2100061 (2021).
- [15] S. A. Moses et al., A race-track trapped-ion quantum processor, *Phys. Rev. X* **13**, 041052 (2023).
- [16] J. F. Kam, H. Kang, C. D. Hill, G. J. Mooney, and L. C. L. Hollenberg, Generation and preservation of large entangled states on physical quantum devices, arXiv (2023), 2312.15170 [quant-ph].
- [17] S. Cao, B. Wu, F. Chen, M. Gong, Y. Wu, Y. Ye, C. Zha, H. Qian, C. Ying, S. Guo, *et al.*, Generation of genuine entanglement up to 51 superconducting qubits, *Nature*, 1 (2023).
- [18] C. H. Bennett, G. Brassard, C. Crépeau, R. Jozsa, A. Peres, and W. K. Wootters, Teleporting an unknown quantum state via dual classical and Einstein-Podolsky-Rosen channels, *Phys. Rev. Lett.* **70**, 1895 (1993).
- [19] D. Bouwmeester, J.-W. Pan, K. Mattle, M. Eibl, H. Weinfurter, and A. Zeilinger, Experimental quantum teleportation, *Nature* **390**, 575 (1997).
- [20] Y.-H. Kim, S. P. Kulik, and Y. Shih, Quantum teleportation of a polarization state with a complete Bell state measurement, *Phys. Rev. Lett.* **86**, 1370 (2001).
- [21] C. H. Bennett and S. J. Wiesner, Communication via one-and two-particle operators on Einstein-Podolsky-Rosen states, *Physical Review Letters* **69**, 2881 (1992).
- [22] K. Wang, X.-T. Yu, S.-L. Lu, and Y.-X. Gong, Quantum wireless multihop communication based on arbitrary Bell pairs and teleportation, *Phys. Rev. A* **89**, 022329 (2014).
- [23] S. Yokoyama, R. Ukai, S. C. Armstrong, C. Sornphiphatphong, T. Kaji, S. Suzuki, J.-i. Yoshikawa, H. Yonezawa, N. C. Menicucci, and A. Furusawa, Ultra-large-scale continuous-variable cluster states multiplexed in the time domain, *Nature Photonics* **7**, 982 (2013).
- [24] S. Olmschenk, D. Matsukevich, P. Maunz, D. Hayes, L.-M. Duan, and C. Monroe, Quantum teleportation between distant matter qubits, *Science* **323**, 486 (2009).
- [25] S. Hermans, M. Pompili, H. Beukers, S. Baier, J. Borregaard, and R. Hanson, Qubit teleportation between non-neighbouring nodes in a quantum network, *Nature* **605**, 663 (2022).
- [26] M. Beverland, V. Kliuchnikov, and E. Schoute, Surface code compilation via edge-disjoint paths, *PRX Quantum* **3**, 020342 (2022).
- [27] E. Bäumer, V. Tripathi, D. S. Wang, P. Rall, E. H. Chen, S. Majumder, A. Seif, and Z. K. Mineev, Efficient long-range entanglement using dynamic circuits, arXiv (2023), 2308.13065 [quant-ph].
- [28] S. Bose, V. Vedral, and P. L. Knight, Multiparticle generalization of entanglement swapping, *Phys. Rev. A* **57**, 822 (1998).
- [29] R. Jozsa, An introduction to measurement based quantum computation, arXiv (2005), quant-ph/0508124 [quant-ph].
- [30] J. Koch, T. M. Yu, J. Gambetta, A. A. Houck, D. I. Schuster, J. Majer, A. Blais, M. H. Devoret, S. M. Girvin, and R. J. Schoelkopf, Charge-insensitive qubit design derived from the Cooper pair box, *Phys. Rev. A* **76**, 042319 (2007).
- [31] K. Wang, X.-T. Yu, S.-L. Lu, and Y.-X. Gong, Quantum wireless multihop communication based on arbitrary Bell pairs and teleportation, *Phys. Rev. A* **89**, 022329 (2014).
- [32] G. Vidal and R. F. Werner, Computable measure of entanglement, *Phys. Rev. A* **65**, 032314 (2002).
- [33] H. Shapourian, K. Shiozaki, and S. Ryu, Partial time-reversal transformation and entanglement negativity in fermionic systems, *Physical Review B* **95**, 165101 (2017).
- [34] M. A. Nielsen and I. L. Chuang, *Quantum Computation and Quantum Information* (Cambridge University Press, 2022).
- [35] P. D. Nation, H. Kang, N. Sundaresan, and J. M. Gambetta, Scalable mitigation of measurement errors on quantum computers, *PRX Quantum* **2**, 040326 (2021).
- [36] G. J. Mooney, G. A. L. White, C. D. Hill, and L. C. L. Hollenberg, Generation and verification of 27-qubit greenberger-horne-zeilinger states in a superconducting quantum computer, *Journal of Physics Communications* **5**, 095004 (2021).
- [37] C. Michelot, A finite algorithm for finding the projection of a point onto the canonical simplex of \mathbb{R}^n , *Journal of Optimization Theory and Applications* **50**, 195 (1986).
- [38] J. A. Smolin, J. M. Gambetta, and G. Smith, Efficient method for computing the maximum-likelihood quantum state from measurements with additive Gaussian noise, *Phys. Rev. Lett.* **108**, 070502 (2012).
- [39] H. Kang and J. F. Kam, teleportation_code_IBM, https://github.com/KangHaiYue/teleportation_code_IBM (2024).
- [40] R. Raussendorf, D. E. Browne, and H. J. Briegel, Measurement-based quantum computation on cluster states, *Physical Review A* **68**, 10.1103/physreva.68.022312 (2003).
- [41] A. G. Fowler, M. Mariantoni, J. M. Martinis, and A. N. Cleland, Surface codes: Towards practical large-scale quantum computation, *Physical Review A* **86**, 10.1103/physreva.86.032324 (2012).

Appendix A: Mathematical details of teleportation

Result A1. Let $|\Phi\rangle = CZ_{1,2}|\phi\rangle_{0,1} \otimes |+\rangle_2$, be a three-qubit quantum state defined on Hilbert space $\mathcal{H}_{0,1,2}$ with $|\phi\rangle_{0,1}$ as an arbitrary two-qubit quantum state rests on qubit 0 and 1 entangled with qubit 2 in the X -basis state $|+\rangle_2$ via Controlled- Z gate, where $|+\rangle := \frac{1}{\sqrt{2}}(|0\rangle + |1\rangle)$ in the computational Z -basis.

If qubit 1 is measured in the X -basis with outcome s , the state $|\phi\rangle_{0,1}$ will be teleported to $|\phi\rangle_{0,2}$ up to the local transformation that depends on the outcome s , yielding

$$|\Phi\rangle^{(\text{Teleported})} = |s\rangle_1 \otimes \underbrace{X_2^{s_1} H_2 |\phi\rangle_{0,2}}_{|\psi\rangle_{0,2}^{(\text{Transformed})}}, \quad (\text{A1})$$

where $s \in \{0, 1\}$.

Proof. In the computational Z -basis, we consider the state $|\phi\rangle$ to be written as

$$|\phi\rangle = \alpha|00\rangle + \beta|01\rangle + \gamma|10\rangle + \delta|11\rangle, \quad (\text{A2})$$

where $\alpha, \beta, \gamma, \delta \in \mathbb{C}$. Hence, the state $|\Phi\rangle$ before teleportation is expressed as

$$\begin{aligned} |\Phi\rangle &= CZ_{1,2}(\alpha|00\rangle + \beta|01\rangle + \gamma|10\rangle + \delta|11\rangle)_{0,1} \frac{(|0\rangle + |1\rangle)_2}{\sqrt{2}} \\ &= \frac{1}{\sqrt{2}}(\alpha(|000\rangle + |001\rangle) + \beta(|010\rangle - |011\rangle) \\ &\quad + \gamma(|100\rangle + |101\rangle) + \gamma(|110\rangle - |111\rangle)). \end{aligned} \quad (\text{A3})$$

Instead of physically measuring in X -basis, a Hadamard gate H is applied before its measurement in the computational Z -basis, where $H|0\rangle = |+\rangle = \frac{1}{\sqrt{2}}(|0\rangle + |1\rangle)$, $H|1\rangle = |-\rangle = \frac{1}{\sqrt{2}}(|0\rangle - |1\rangle)$. For consistency with the rest of the work, we also change the basis before measurements in this proof. Therefore, the state before measurement becomes

$$\begin{aligned} H_1 |\Phi\rangle &= \frac{1}{2} |0\rangle_1 \otimes ((\alpha + \beta)|00\rangle + (\alpha - \beta)|01\rangle \\ &\quad + (\gamma + \delta)|10\rangle + (\gamma - \delta)|11\rangle)_{0,2} \\ &\quad + \frac{1}{2} |1\rangle_1 \otimes ((\alpha - \beta)|00\rangle + (\alpha + \beta)|01\rangle \\ &\quad + (\gamma - \delta)|10\rangle + (\gamma + \delta)|11\rangle)_{0,2}, \end{aligned} \quad (\text{A4})$$

which reduces to

$$\begin{aligned} H_1 |\Phi\rangle &= \frac{1}{2} |0\rangle_1 \otimes H_2(\alpha|00\rangle + \beta|01\rangle + \gamma|10\rangle + \delta|11\rangle) \\ &\quad + \frac{1}{2} |1\rangle_1 \otimes X_2 H_2(\alpha|00\rangle + \beta|01\rangle + \gamma|10\rangle + \delta|11\rangle). \end{aligned} \quad (\text{A5})$$

When the measurement of qubit 1 in Pauli- X basis is carried out, the superposition of state $|0\rangle$ and $|1\rangle$ on qubit 1 collapses to $|s\rangle$,

$$M_{1,s} H_1 |\Phi\rangle = |s\rangle_1 \otimes X_2^s H_2 |\phi\rangle_{0,2}. \quad (\text{A6})$$

where the measurement operator $M_{i,x}$ projects the state on qubit i of a multi-qubit state $|a\rangle$ in the $|x\rangle$ direction and $x \in \{0, 1\}$, which is an eigenstate of the Pauli- Z operator. When acted on an arbitrary state $|a\rangle$, it is denoted as $M_{i,x}|a\rangle = \frac{|x\rangle_i \langle x|_i}{\|\langle x|a\rangle\|^2} |a\rangle$. The state $|\phi\rangle_{0,2}$ now carries local transformation $X_2^s H_2$ [41]. Therefore, we have shown that for arbitrary two-qubit state $|\phi\rangle$, the claim as stated in Result A1 holds. Or equivalently,

$$M_{1,s} H_1 \underbrace{(CZ_{1,2} |\phi\rangle_{0,1} \otimes |+\rangle_2)}_{|\Phi\rangle} = |s\rangle_1 \otimes \underbrace{X_2^s H_2 |\phi\rangle_{0,2}}_{|\psi\rangle_{0,2}^{(\text{Transformed})}}. \quad (\text{A7})$$

□

Result A2. Let $|\Phi\rangle = \left(\prod_{i=1}^{n-2} CZ_{i,i+1} \right) \otimes |+\rangle_{j+1} \otimes |\phi\rangle_{0,1}$

be a n -qubit quantum state with $|\phi\rangle_{0,1}$ as an arbitrary two-qubit quantum state rest on qubit 0 and 1 entangled with other qubits in the X -basis state $|+\rangle$ via CZ gate in a path, where CZ is the two-qubit entangling Controlled- Z gate.

If all intermediate qubits from 1 to $n-2$ are measured in the X -basis with outcome $\vec{s} = (s_1, s_2, \dots, s_{n-2})^T$, the state $|\phi\rangle_{0,1}$ will be teleported to qubit 0 and $n-1$ up to the local transformation that depends on the outcome \vec{s} , yielding

$$|\Phi\rangle^{\text{Teleported}} = \left(\prod_{i=1}^{n-2} X_{n-1}^{s_i} H_{n-1} \right) |\phi\rangle_{0,n-1} \otimes |\vec{s}\rangle, \quad (\text{A8})$$

where $\vec{s} \in \{0, 1\}^{\otimes n-2}$.

Proof. From Result A1, we modify Equation A7 by changing labels and adding a new qubit to the system, such that the Hilbert space concerning the new equation is $\mathcal{H}_{N-3} \otimes \mathcal{H}_{0,N-2,N-1}$,

$$\begin{aligned} M_{n-2,s_{n-2}} H_{n-2} CZ_{n-2,n-1} |s_{n-3}\rangle \otimes |\phi\rangle_{0,n-2} \otimes |+\rangle_{n-1} \\ = |s_{n-3}\rangle \otimes |s_{n-2}\rangle \otimes X_{n-1}^{s_{n-2}} H_{n-1} |\phi\rangle_{0,n-1}, \end{aligned} \quad (\text{A9})$$

The newly added qubit $n-3$ is in the state $|s_{n-3}\rangle$ with $s_{n-3} \in \{0, 1\}$, which is not coupled to any other qubits. Without loss of generality, we let

$$|s_{n-3}\rangle \otimes |\phi\rangle_{0,n-2} = |s_{n-3}\rangle \otimes X_{n-2}^{s_{n-3}} H_{n-2} |\phi'\rangle_{0,n-2}, \quad (\text{A10})$$

where $|\phi'\rangle$ is some two-qubit state can directly transform to $|\phi\rangle$ depends on the value of the newly added qubit, s_{n-3} . After change the labels, we substitute Equation A7 into RHS of Equation A10, yielding

$$\begin{aligned} |s_{n-3}\rangle \otimes |\phi\rangle_{0,n-2} = M_{n-3,s_{n-3}} H_{n-3} (CZ_{n-3,n-2} |\phi'\rangle_{0,n-3} \\ \otimes |+\rangle_{n-2}), \end{aligned} \quad (\text{A11})$$

which is substituted back to LHS of Equation A9. It is now clear that we can interpret $|s_{n-3}\rangle$ as the state collapsed after measuring in Pauli X -basis. Also, by applying the

same trick that changes the label of qubit $n - 2$ to $n - 1$, Equation A10 becomes

$$|s_{n-3}\rangle \otimes |\phi\rangle_{0,n-1} = |s_{n-3}\rangle \otimes X_{n-1}^{s_{n-3}} H_{n-1} |\phi'\rangle_{0,n-1}, \quad (\text{A12})$$

which is substituted back to RHS of Equation A9. By looping over the process of adding new qubits with the state $|s_{n-4}\rangle, |s_{n-5}\rangle, \dots, |s_1\rangle$ to both sides of Equation A9 and recursively substituting Equation A11 to the LHS of Equation A9 and Equation A12 to RHS of Equation A9, we obtain

$$\begin{aligned} |s_1 \cdots s_{n-2}\rangle \otimes \left(\prod_{i=1}^{n-2} X_{n-1}^{s_i} H_{n-1} \right) |\phi^{(n-2)}\rangle_{0,n-1} &= \left(\prod_{i=1}^{n-2} M_{i,s_i} H_i C Z_{i,i+1} \right) \bigotimes_{j=2}^{n-1} |+\rangle_j \otimes |\phi^{(n-2)}\rangle_{0,1} \\ &= \left(\prod_{i=1}^{n-2} M_{i,s_i} H_i \right) \left(\prod_{j=1}^{n-2} C Z_{j,j+1} \right) \bigotimes_{k=2}^{n-1} |+\rangle_k \otimes |\phi^{(n-2)}\rangle_{0,1}, \end{aligned} \quad (\text{A13})$$

where the Controlled-Z operators are grouped to the right since they all commute with the Hadamard and measurement projection gates acting independently on different qubits. Similarly to Equation A12, we let $|\phi\rangle$ be a transformation of some state $|\phi^{(n-2)}\rangle$ after $n - 2$ iterations,

$$T : S \rightarrow \mathcal{H}', |\phi\rangle = (X^{s_{n-2}} H) \cdots (X^{s_1} H) |\phi^{(n-2)}\rangle, \quad (\text{A14})$$

where $S \subset \mathcal{H}'$ is some subset of the Hilbert space \mathcal{H}' , and recall that \mathcal{H}' is spanned by all possible two-qubit state satisfying $\langle \phi | \phi \rangle = 1$. Suppose S takes the maximal domain $S = \mathcal{H}'$, then the image of T is in some $D \subset \mathcal{H}'$. However, we know $D = \mathcal{H}'$ is strictly the full Hilbert space since $|\phi\rangle$ is set to be arbitrary. Thus, by the unitarity of T , the image of T^{-1} must be equal to \mathcal{H}' . Or equivalently, the choice of $|\phi^{(n-2)}\rangle$ is also arbitrary. Therefore, we have proved Result A2. \square

Appendix B: Optimal paths search algorithm

Algorithm B1 Optimal paths search algorithm

Input: A weighted graph G with vertex set $V(G)$ and edge set $E(G)$, such that the edges are the available connections between the qubits weighted using one of the protocols discussed in Section IV.

Output: The best m paths with n qubits.

Let $P = \{P_n | P_n \subseteq G\}$ be the set of paths that are all subgraphs of G with n vertices/qubits.

Let $S = \emptyset$

for $P_n \in P$ **do:**

$k = 1$

for $e_{ij} \in E(P_n)$ **do:**

$k \leftarrow w(e_{ij})k$

end for

$S \leftarrow S \cup \{(k, P_n)\}$

end for

Let $T = (S, \leq)$ be the ordered set of S such that $\forall (k_1, P_{n_1}), (k_2, P_{n_2}) \in S, k_1 \leq k_2 \iff (k_1, P_{n_1}) \leq (k_2, P_{n_2})$.

Let T' be the last m elements of T , where $P_n^{(\text{opt})} \in T'$ is the last element.

Output T'
